

# An Optofluidic Guided-Mode Resonance Platform for Binding Kinetics Applications

Meryem Beyza Avci, Furkan Kocer, Nimet Yildirim-Tirgil, Chanunthorn Chananonwathorn, Tossaporn Lertvanithpol, Mati Horprathum, Uraivan Waiwijit, Sakoolkan Boonruang, Khwanchai Tantiwanichapan, and Arif E. Cetin

**Abstract**— Guided mode resonance (GMR) sensors have emerged as transformative tools in sensing technology, offering exceptional sensitivity, selectivity, and real-time, label-free detection capabilities across diverse applications, including medical diagnostics and environmental monitoring. Their miniaturization potential, cost-effective manufacturing, and wide dynamic range make GMR sensors highly versatile and commercially attractive. In this study, we present an optofluidic GMR platform tailored for real-time analysis of biomolecular interactions without the need for optical labels. The platform integrates a custom-built inverted microscopy system, a high-resolution multi-spectrometer setup with a spectral resolution of 0.15 nm, and an automated multi-pump fluid control system, enabling precise and efficient monitoring of binding kinetics between biomolecules. Key outcomes include a refractive index sensitivity of 201.73 nm/RIU and a demonstrated detection limit of 0.15 ng/mL for IgG protein, emphasizing the platform's suitability for highly sensitive biodetection applications. Additionally, the automated flow methodology enhances efficiency and reproducibility by streamlining chip preparation, ligand/analyte incubation, and post-experiment cleaning, minimizing manual intervention and human error. The self-cleaning feature ensures contamination-free operation, facilitating seamless multi-use experiments. Furthermore, we determined the association constant during the binding of protein A/G and IgG, underscoring the platform's applicability to real-time binding kinetics studies. These results establish our optofluidic GMR platform as a robust and precise tool for advancing the understanding of complex biomolecular processes.

**Index Terms**— Binding dynamics, Guided mode resonance, Label-free biosensing, Nanotechnology, Optofluidic

## I. INTRODUCTION

IN recent years, guided mode resonance (GMR) sensors have emerged as a promising technology with immense potential in various sensing applications [1], [2]. In 1992, Magnusson and Wang were the first to propose the utilization of the GMR effect for sensor applications, unveiling GMR filters whose characteristics could be adjusted by altering resonance structure parameters such as thickness and refractive index [3]. Building upon the initial discovery by Magnusson and Wang, Tibuleac *et al.* and Wawro *et al.* further expanded the GMR technology landscape by introducing novel GMR biosensor designs and exploring their integration with optical

fibers, opening new avenues for sensor applications [4], [5]. This evolution marked a significant advancement in the field, demonstrating the versatility and broad applicability of GMR sensors beyond the traditional settings. These sensors offer a unique combination of high sensitivity, selectivity, miniaturization, real-time detection, and label-free operation [6]. Such attributes have propelled GMR sensors to the forefront of research and development, driving their integration into diverse fields, ranging from environmental monitoring to medical diagnostics and industrial process control [7]–[11].

One of the fundamental strengths of GMR sensors lies in their exceptional sensitivity to minute changes in the refractive index of the surrounding medium [12]. This remarkable sensitivity enables the detection of even the most subtle variations in the analyte concentration or physical properties, such as temperature or pressure [13]. By leveraging this sensitivity, GMR sensors provide valuable insights into dynamic processes and enable accurate measurements with high precision. Furthermore, GMR sensors exhibit remarkable selectivity, thanks to their ability to resonate strongly only at specific wavelengths or within a narrow spectral range [14]. This unique feature enables selective detection of target analytes or substances, minimizing interference from other components present in the sample. Such selectivity enhances the reliability and accuracy of the measurements, making GMR sensors particularly valuable in complex and multi-component environments [15]. The miniaturization capability of GMR sensors is another key advantage that has sparked considerable interest in recent

This work was supported by the Development of International Cooperation Network on Science Technology and Innovation, Program Management Unit for Human Resources & Institutional Development, Research and Innovation (PMU-B) of Thailand (which is under the Program 16: Partnership Initiative Fund: S&T) Grant No. B16F640194, National Higher Education Science Research and Innovation Policy Council.

Meryem Beyza Avci, Furkan Kocer, and Arif E. Cetin are with the Izmir Biomedicine and Genome Center, Balçova, Izmir 35340, Turkey.

Arif E. Cetin is with the Izmir International Biomedicine and Genome Institute, Dokuz Eylül University, Balçova, Izmir 35340, Turkey (Corresponding Author, e-mail: arifengin.cetin@ibg.edu.tr).

Nimet Yildirim-Tirgil is with the Department of Biomedical Engineering, Ankara Yildirim Beyazıt University, Keçioren, Ankara 06010, Turkey.

Chanunthorn Chananonwathorn, Tossaporn Lertvanithpol, Mati Horprathum, Uraivan Waiwijit, Sakoolkan Boonruang, and Khwanchai Tantiwanichapan are with the Spectroscopic and Sensing Devices Research Group (SSDRG), Opto-Electrochemical Sensing Research Team (OEC), National Electronics and Computer Technology Center (NECTEC), Pathum Thani 12120, Thailand.

years. These sensors can be fabricated using micro- and nano-fabrication techniques, allowing for their integration into compact devices [16]. As a result, GMR sensors hold great potential for portable and wearable sensing applications, where their small form factor and low power requirements enable on-the-go monitoring and personalized healthcare [17], [18].

Moreover, GMR sensors offer real-time and label-free detection, operating based on changes in optical properties, such as wavelength shift or intensity modulation [19]. This eliminates the need for additional labels or chemical modifications, simplifying the sensing process and enabling rapid and continuous measurements. The ability to obtain real-time data is crucial in numerous applications, including monitoring environmental pollutants, tracking biological processes, and ensuring the quality and safety of industrial processes. In addition to their inherent strengths, GMR sensors boast a wide dynamic range, allowing for accurate detection across a broad range of analyte concentrations [20]. From low to high levels, GMR sensors maintain their sensitivity, offering versatility in diverse sensing applications. Furthermore, these sensors can be designed to operate across different parts of the electromagnetic spectrum, such as visible, near-infrared, or mid-infrared, making them compatible with a wide range of light sources and detectors [21]. Lastly, the cost-effective manufacturing of GMR sensors through standard semiconductor fabrication techniques has accelerated their commercialization potential [22]. This affordability promotes large-scale deployment and integration into various sectors, facilitating the translation of GMR sensor technologies from laboratory to practical applications [23].

When compared with existing optical sensing technologies, GMR platforms demonstrate competitive advantages alongside certain trade-offs. While Surface Plasmon Resonance (SPR) sensors, as highlighted in the literature, achieve superior refractive index sensitivity and ultra-low detection limits in the range of 10–100 pg/mL [37]–[39], GMR sensors offer enhanced thermal and chemical stability due to their dielectric-based construction [40], [41]. Optofluidic systems, such as those detailed by Wu et al., provide real-time, in situ analysis with increased sensitivity through microfluidic integration [42]. However, GMR sensors' narrower spectral bandwidth results in a higher figure of merit (FOM), making them well-suited for precision-demanding applications [43], [44]. Emerging technologies such as plasmonically induced transparency (PIT) in graphene nanostructures have demonstrated remarkable potential for ultra-high sensitivity and spectral tunability [45]. However, these PIT-based devices often require complex fabrication processes and offer limited scalability. In contrast, GMR platforms support cost-effective and scalable fabrication methods, such as atomic layer deposition (ALD), enabling consistent and reproducible sensor production [41]. Similarly, multi-band optically tunable perfect light absorbers [46], [47] and metamaterial absorbers [47] have shown notable versatility, though their integration with microfluidic platforms remains less developed compared to the operational flexibility of GMR sensors. While the refractive index sensitivity of the GMR platform may not exceed that of SPR or PIT-based systems, its unique combination of robustness, adaptability, and

cost-efficiency makes it a promising alternative for biosensing applications, particularly in challenging environments and resource-limited settings.

In this article, we introduced a compact and fully-automated optofluidic GMR platform designed to facilitate the real-time investigations of biomolecular interactions in a label-free manner. The platform integrates an inverted microscopy system equipped with linearly polarized illumination alongside a multi-spectrometer setup supporting a high spectral resolution, e.g., 0.15 nm, which is critical for accurately monitoring spectral variations. A multi-pump system, regulated by a flow sensor, enables precise control over the fluid flow, allowing for the implementation of various protocols within the platform. A key feature of our optofluidic platform is its automated flow methodology, which facilitates the preparation of the chip surface for sensing tests, the incubation of ligands and analytes, and the self-cleaning of the system following each protocol. This automation significantly improves the efficiency, accuracy, and repeatability of sensor-based assays, reducing manual intervention and the associated risk of operator errors. The self-cleaning ability maintains a contamination-free environment between experiments further enhancing the platform's utility. To enhance the functionality of our optofluidic GMR platform, we have developed a user-friendly software that operates with the system hardware, designed to simultaneously control the optofluidic components, e.g., acquisition of spectral data from the GMR substrate as it interacts with various analytes, and execution of protocols for surface modification, and analyte delivery. The primary function of the software includes the generation and post-processing of these spectral raw data, transforming them into meaningful real-time sensing information. The software's capabilities extend to the analysis of binding kinetics, where it computes the binding constants that govern the interactions between the ligands and the analytes under study.

Figure 1 shows the photograph of the optofluidic GMR platform along with the system software executed on a notebook, and the schematics of the system components. To optimize data quality while reducing background noise and consolidating all hardware components, we have enclosed the system within a protective case, which also creates an ideal dark environment for optimal conditions for the spectral measurement based on light transmission.

The platform comprises four essential components:

- i. **Optics Module:** In this module, a broadband halogen lamp illuminates the GMR chips, while a triple-spectrometer system captures and measures the transmitted light, allowing for the analysis of waveguide modes created by the GMR structure.
- ii. **Microfluidics Module:** This module integrates a one-channel polydimethylsiloxane (PDMS)-based flow cell and a microcontroller-driven four-piezoelectric pump system. This module ensures precise delivery of analytes to the functionalized sensing surface, enabling real-time monitoring of binding events, and system cleaning.
- iii. **Software Module:** This module offers a user-friendly graphical user interface (GUI) for simultaneous control of optical and microfluidic components. It also incorporates a data-processing algorithm that uses the real-time transmission

spectra of the GMR structures to calculate binding parameters. System control and data acquisition are achieved using a notebook, with communication between different modules established via USB (universal serial bus) connectivity.

For the label-free refractive index sensing experiments, we utilized a GMR-based chip, leveraging its aforementioned advantages.

iv. **GMR Chip:** The chip consists of a planar waveguide with a periodic structure. Leveraging the highly sensitive nature of the GMR chip, the platform supports a refractive index sensitivity of  $\sim 201.73$  nm/RIU (refractive index unit), which is advantageous for label-free biosensing applications. This waveguide structure exhibits a well-defined and isolated resonances with a linewidth of  $\sim 40.5$  nm.

In order to demonstrate the applicability of our optofluidic GMR platform in real-time binding kinetic analyses, we investigated the interactions between protein A/G and protein IgG, and successfully determined the parameter governing the association phase. Based on our label-free biosensing experiments involving protein mono- and bilayers, achieving a high limit-of-detection of 0.15 ng/mL for protein IgG. We believe our optofluidic GMR platform with high spectral resolution embodies a significant technological advancement in biosensing, featuring a fully automated sensing mechanism for real-time binding kinetics analyses. It integrates self-cleaning functionality and consolidates hardware control and data post-processing within a singular software framework, enhancing operational efficiency and analytical precision. This system represents a comprehensive solution for the real-time analysis of biomolecular interactions, which could be a strong candidate in the field of biosensing.

## II. MATERIALS AND METHODS

### A. Optical Setup of the Optofluidic GMR Platform

The Optics Module employs an inverted microscopy setup with a spectrometer-based read-out scheme (Figure 1). To attain high sensitivity, we engineered a high-resolution spectrometer system consisting of three simultaneously operating spectrometers that evenly disperse the spectral region of interest. Figure 5 shows the snapshot of the GUI demonstrating the spectral range of each spectrometer that are highlighted with different colors, e.g., blue, green and red. This approach yields a high optical resolution of 0.15 nm, which is critical for sensitive label-free and real-time binding kinetics applications, especially when confronted with low analyte concentrations. The optical configuration of this module employs a broadband halogen light source coupled with a fiber to illuminate the GMR chip. The incident light is initially collimated with a fiber collimator. To selectively excite the waveguide mode while eliminating potential interference from the unwanted modes, a linear polarizer is employed, ensuring the incident light is polarized in parallel with the periodic structure. To exclusively illuminate the GMR structure within the one-channel microfluidics and prevent interactions with GMR structures outside this channel, a shutter is employed shrinking the diameter of the light source impinging on the GMR structure to match it with the channel width. The transmitted light from

the GMR chip is directed towards the fiber collimator via an achromatic lens, which subsequently routes the transmitted light to the three spectrometers via a trifurcated fiber.

### B. Piezoelectric-Pump System

The Microfluidics Module utilizes a piezoelectric pump system for analyte delivery to the sensor surface via the flow cell (Figure 1). Control of the four piezoelectric pumps is achieved through a microcontroller, allowing for the adjustment of flow rates by varying the supplied voltage to the pumps. By applying voltage levels of 250 peak-to-peak voltage (Vpp) at a constant frequency, such as 100 Hz, the desired flow rates could be attained. A 4-in-1-out manifold, containing four valves that are controlled by the microcontroller, selectively delivers samples to the GMR chip's surface. Simultaneously, a flow sensor works in conjunction with the chosen pump and its associated valve to maintain a continuous flow rate. The spectrometers are directly controlled by a notebook utilizing device driver libraries, while it manages the microcontroller to operate the pumps, valves, and flow sensor. The microcontroller adjusts its voltage via I2C communication within a range of 0 to 31 bytes, where these bytes correspond to a voltage mapping from 0 to 250 Vpp, and it employs on/off voltage signals, controlled by four relays, to manipulate the valves. The flow rate is controlled through a proportional-integral-derivative (PID) controller. A derivative filter is applied to the derivative term of the PID controller. This aids in smoothing sharp changes in the control signal (voltage output), and reduces the impact of the noise on the derivative term. However, the effectiveness of the filter depends on the characteristics of the control system and the nature of the noise it deals with. Furthermore, a smoothing factor is applied to the output of the PID controller to achieve smoother changes in the pump voltage. This helps reduce sudden voltage changes that could lead to instability or mechanical stress on the pumps, similar to the effect of the derivative filter. The output limits were defined to ensure that the pumps do not operate outside a specified voltage range. This practice is essential for safety, and to ensure that the pumps function within their designated operational limits. In the PID controller, the feedback mechanism between the pump and the flow rate sensor through the microcontroller was modelled as a first order system. First-order systems are fundamental models in control theory, describing the relationship between input and output through a first-order differential equation. These equations encapsulate the system's dynamics by accounting for the first derivative of the output concerning time. Essentially, they characterize systems where higher-order derivatives are absent, thereby illuminating the system's responsiveness to input signals over time. In our PID controller, each component of PID contributes distinct mathematical computations to manipulate the error signal,  $e(t)$ , thereby influencing the controller's output. We modelled our PID controller with the following formula, which is schematically illustrated in Figure 4A:

$$u(t) = K_p e(t) + K_i \int_0^t e(t) dt + K_d \frac{\partial e(t)}{\partial t} \quad (1)$$

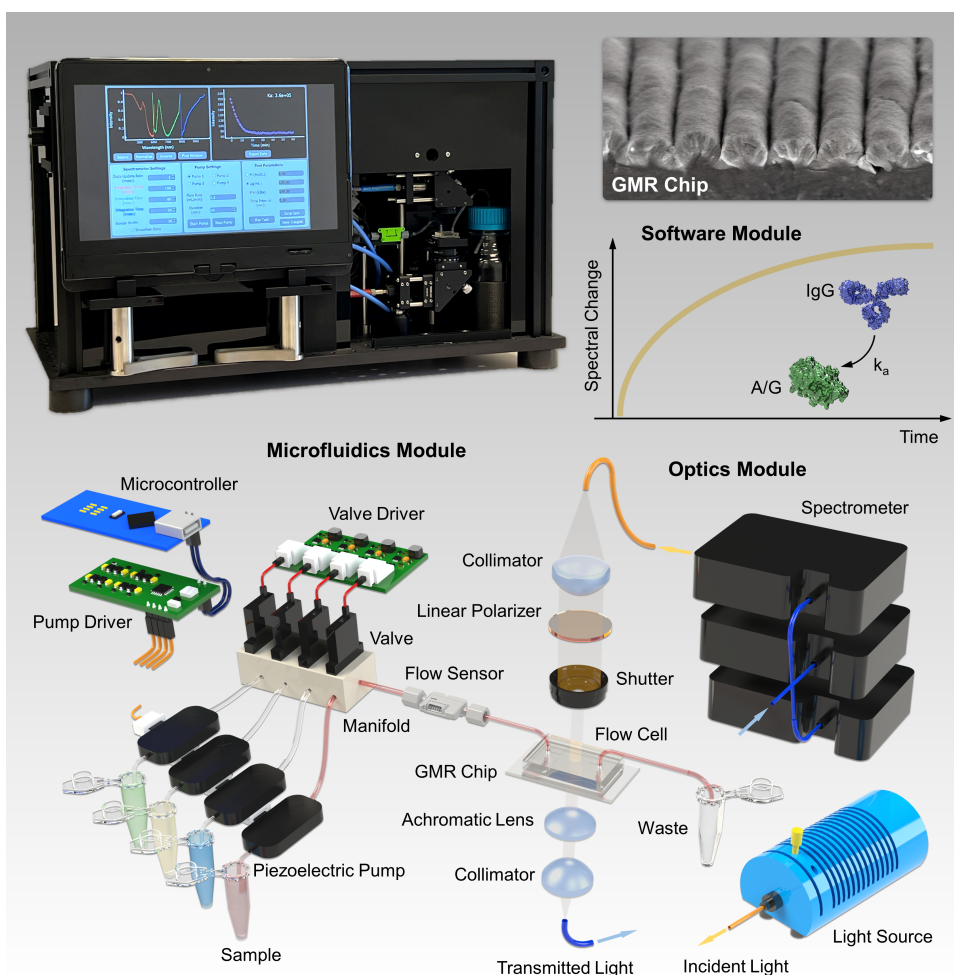


Fig. 1. Photograph of the optofluidic GMR platform with a built-in notebook for operating the system and the schematic illustration of its hardware and software components for analyzing the binding kinetics of biomolecular interactions. The platform is composed of three modules, e.g., Optics, Microfluidics and Software modules, along with the fourth component, e.g., a GMR Chip. The figure inset displays the SEM image of the GMR structure.

where  $K_p$  is the Proportional term, generating an output proportional to the current error magnitude. The integral term,  $K_i$ , considers both the error magnitude and duration, ensuring precision over prolonged periods. Conversely, the derivative term factors,  $K_d$ , in the error's rate of change, offering insight into future errors based on the present trends. Collectively, these terms manipulate the control actions, enabling error correction and system stabilization for a stable flow. Figure 4B shows the flow rate (black) of a single pump measured with the flow sensor for a period of 15 min duration for different set values (red), e.g., in the range of 0.1 mL/min to 4 mL/min. Our PID controller ensures a stable flow with only 5% standard deviation. In order for a robust surface functionalization and stable biomolecular interactions between ligands and analytes, we performed the real-time binding kinetic experiments under 0.1 mL/min flow rate [24], [25].

### C. Fabrication of the GMR chips

As shown in Figure 2A, GMR structures were fabricated using the nanoimprint method [26]. The procedural sequence begins with the realization of a master mold (i). For the mold

fabrication, the surface of a glass substrate was coated with a photoresist, and the sinusoid patterns were realized through laser interference lithography. The photoresist surface was then coated with tantalum oxide ( $TaO_2$ ) to realize a more solid master mold surface. Following this, the master mold was used to shape the PDMS mold (ii). Subsequently, the PDMS grating structure (iii) serves as the primary mold for the production of the GMR structures. In the next step, a silicon-on-glass (SOG) layer was spin-coated onto the glass substrate. The grating pattern inherited from the PDMS mold was transferred onto the SOG layer through the nanoimprinting process (iv), resulting in the diffraction grating patterns observed in the GMR structure (v). Following this step, the waveguide layer was fabricated via sputtering, where tantalum (Ta) was used as the target material, with an operational pressure of 10 mTorr or 20 mTorr of Oxygen + Argon ( $O_2+Ar$ ) within the chamber (vi). As shown in Figure 2C, fabrication was processed for the following device parameters, e.g., the thickness of the  $TaO_2$  layer is 190 nm, grating height is 100 nm, and the thickness of the SOG layer is 500 nm, where the overall GMR structure was manufactured on a glass substrate with a thickness of 1 mm. The GMR structure was engineered to have

a resonant wavelength around 600 nm, i.e., the corresponding grating period was chosen as  $\sim 380$  nm. In our fabrication method, the grating is limited by the capabilities of the master mold fabricated by laser interference lithography [27]. Figure 2B-inset shows the photograph of a 25 mm  $\times$  25 mm GMR chip. Figure 2E shows the scanning electron microscope (SEM) images of the fabricated TaO<sub>2</sub>-based GMR structures, demonstrating the quality of our fabrication method over a large area.

### III. RESULTS AND DISCUSSION

#### A. Optical Properties of the GMR Chip

In order to investigate the underlying physical mechanism responsible for the guided-mode resonance supported by the dielectric structure, we conducted finite-difference time-domain (FDTD) simulations. In the simulations, the unit cell comprises a single waveguide, which consists of a triangular substrate with triangular cladding. Periodic boundary conditions were used along the plane of the waveguide (*xy*-plane) to model the periodic behavior of the triangular column structure. Perfectly matched layer boundary conditions were used along the direction of the illumination source (*z*-axis). The refractive index values for the constituting structures were determined via ellipsometry. In the simulations, for TaO<sub>2</sub> and SOG layers, we used the refractive index values of 1.996 and 1.52, respectively. SOG exhibits excellent transparency in the visible to near-infrared range, with minimal absorption at the operating wavelengths of the GMR structure, ensuring efficient transmission of light. Its refractive index, being lower than that of the TaO<sub>2</sub> thin film layer, enables the formation of a high refractive index contrast that is critical for the waveguide resonance. Additionally, SOG's optical properties, such as its low optical loss and thermal stability, contribute to the overall reliability and robustness of the GMR chip. The substrate's role is not only to provide mechanical support but also to enable effective light diffraction and confinement, facilitating the guided-mode resonance. TaO<sub>2</sub> is transparent in the visible to near-infrared range, ensuring minimal optical loss and high transmission. Its high refractive index, combined with the lower refractive index of the SOG substrate, enables strong light confinement within the waveguiding layer, which is essential for the guided-mode resonance. The thickness and refractive index of the TaO<sub>2</sub> layer directly influence the resonance wavelength, as they determine the waveguide's optical properties. Additionally, TaO<sub>2</sub>'s thermal and environmental stability ensure consistent performance under varying experimental conditions, making it a robust material for GMR-based sensing applications.

In the simulations, a mesh size of 0.5 nm was selected for discretization along all directions. In accordance with the experimental configuration, an *x*-polarized light source was used to illuminate the dielectric structure. Figure 2B-inset illustrates the schematics depicting the axes, along with the polarization and propagation direction of the incident light source. Figure 2B shows the experimental (white) and calculated transmission (black) responses supported by the GMR structure. The spectral positions of the transmission dips

coincide well, while the experimental response has a wider linewidth, e.g.,  $\sim 40.58$  nm, due to the fabrication tolerances. To eliminate the effect of the spectral shape of the halogen light source on determining the linewidth of the optical modes supported by the GMR structure, the corrected transmission spectra were determined by dividing the light transmitted from the waveguide by the source response. Figure 2D displays the cross-sectional profile of the nearfield intensity distribution (magnitude of the electric field) of the waveguide system. GMR is an optical-based device known for its thin film structure, featuring a surface covered with finely patterned nano-sized gratings on a substrate material, and these intricate patterns exhibit remarkable light diffraction properties. The GMR structure incorporates diffractive gratings engraved onto a substrate material, specifically SOG here, which possesses a lower refractive index compared to the thin film coating made of TaO<sub>2</sub>. When light is directed onto the GMR structure, the thin film structure reveals its waveguide characteristics, indicating that light can be confined or reflected within the thin film layer when its propagation constant through the diffracted wave aligns with the waveguide mode. Within the thin film TaO<sub>2</sub>, light undergoes bidirectional propagation. Consequently, this waveguide mode can lead to reflection or transmission through the thin film layer. Reflected light, at the angle of reflection, undergoes constructive interference, resulting in the emergence of a peak in the reflectance spectrum at a specific wavelength, known as the resonance wavelength. In contrast, transmitted light, at the angle of incidence, experiences destructive interference, leading to minimal transmittance at the resonance wavelength. Resonance wavelength of the GMR structure depends on the refractive index of the thin film material, substrate material, and the surrounding medium covering its surface.

#### B. Limit-of-Detection of the GMR Structure

To demonstrate the sensing capability of the GMR structures, we initially conducted sensing experiments with bulk refractive index solutions using various water-ethanol mixtures within the range of 0-80%, resulting in a refractive index range of 1.333 – 1.3658. Figure 3A depicts the spectral position of the transmission dip for each bulk solution, where the squares represent the mean values, and the error bars reflect double the standard deviation of five independent experiments. Through a linear fit to the experimental data  $\lambda = 201.73n - 380.61$ , we determined the refractive index sensitivity as  $S = \Delta\lambda/\Delta n = \sim 201.73$  nm/RIU (refractive index unit).

To further demonstrate the sensing capability of the GMR platform, we performed label-free detection of protein mono and bilayers. In this context, we utilized protein A/G and protein IgG, and analyzed their binding characteristics. Our biosensor platform utilizes a surface modification technique that relies on the physical attachment of analytes to the sensing surface through physical adsorption, e.g., physisorption [28]. Here, the flow cell was employed to deliver the analytes to the sensing surface. Before the analyte/ligand analysis, the chip surface was rinsed with acetone, isopropanol, and DI-water, and dried with nitrogen gas. The chips were then introduced

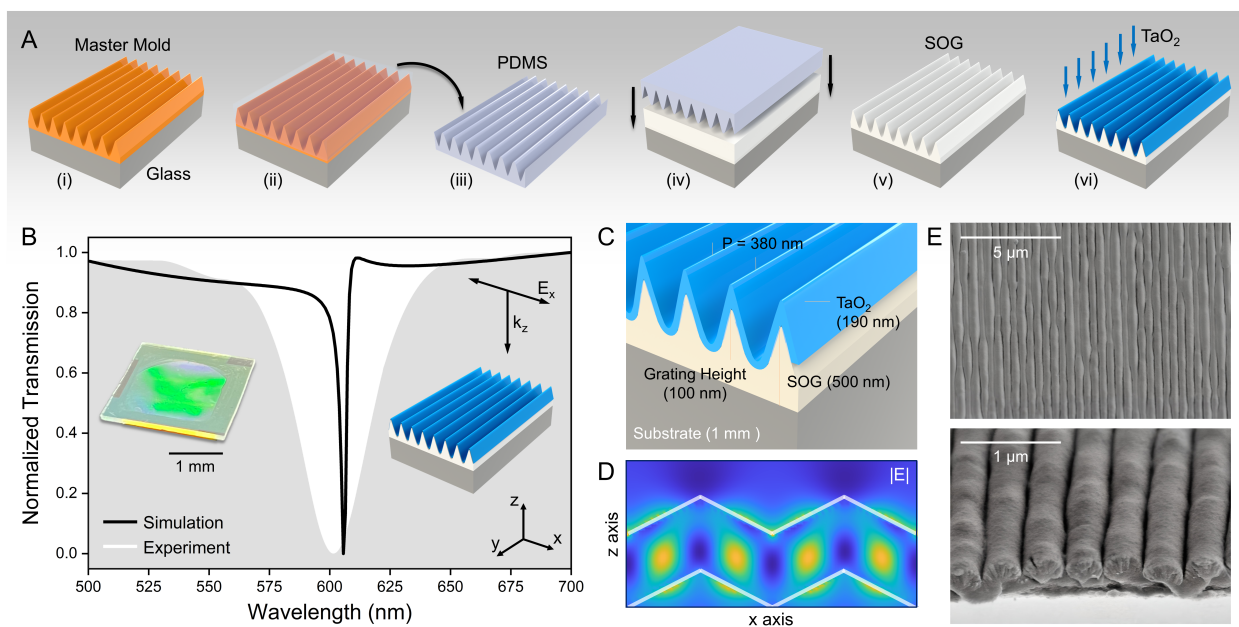


**Fig. 2.** (A) Fabrication steps for the GMR structure. (B) Experimental (white curve) and calculated (black curve) transmission spectra of the GMR structure. Figure inset shows the photograph of a GMR chip. Figure also displays the direction of the polarization and the propagation of the incident light source. (C) Device parameters of the GMR structure. (D) Cross-sectional nearfield profile (magnitude of the electric field) of the GMR structure calculated at the transmission dip. (E) SEM images of the fabricated GMR structures.

into an ultraviolet ozone cleaner. Finally, they were rinsed with isopropanol and DI-water, and dried with nitrogen gas. This cleaning methodology makes the surface more hydrophilic. For analyte attachment on the sensing surface, we flowed the solutions with a flow rate of 0.1 mL/min. With the use of a slow and controlled flow instead of manual pipetting that could result in random bimolecular attachments, GMR surface was uniformly coated for the binding tests, which ensures test repeatability. The surface modification process begins with the delivery of protein A/G to the surface. Protein A/G is a fusion protein that possesses binding sites of both protein A and protein G, and it exhibits a high affinity for the Fc region of the immunoglobulin (IgG) [29]. Subsequently, IgG proteins were introduced and attached to the A/G-coated sensing surface through their Fc region, forming a Y-shaped structure as schematically illustrated in Figure 3C-inset.

Figure 3B shows the transmission resonance supported by the GMR structure after the attachment of monolayer and bilayer protein. The data presented in this figure were processed and smoothed using the Savitzky–Golay filter, which effectively reduces noise while preserving key spectral features for accurate analysis. Ambient light interference, a major external source of noise, was mitigated by enclosing the system in a black casing to block stray light and ensure consistent measurements. Internally, mechanical vibrations that could affect the spectral stability were minimized by mounting the system on vibration-isolating Sorbothane feet, providing a stable base for the experimental setup. Another critical factor contributing to noise is the resolution of the spectrometer. In our system, we carefully balanced the resolution of the spectrometer with the acquisition speed to optimize spectral quality while keeping the noise at a manageable level. For simplifying spectral data

processing, we utilized the 1-Transmission spectrum in our biosensing experiments. The transmission resonance, initially located at 601.49 nm (black curve), shifted by 4.2 nm to 605.69 nm after the attachment of 100 μg/mL protein A/G (green curve). The functionalization of the sensing surface with 100 μg/mL protein IgG further shifted the transmission resonance by an additional 10.24 nm (total shift = 14.44 nm), resulting in a wavelength of 615.93 nm (blue curve).

Traditionally, the impact of the biomass accumulating on the sensing surfaces on the optical properties of the sensing substrate is evaluated by monitoring changes in the maxima or minima of the optical features. However, when dealing with low analyte concentrations, this conventional approach faces a limitation in spectral resolution as it relies solely on a single spectral location. In simpler terms, it struggles to generate adequate spectral variations required for precise measurement of refractive index changes on the sensing surface. To address this challenge, we have devised an alternative approach. Here, instead of exclusively monitoring the spectral shift of the transmission resonance, we have integrated the transmission response within a specific spectral window. This strategy takes into account the collective spectral shifts occurring across multiple wavelengths [30]. The integral window used in our calculations, which has a width of 35 nm, is highlighted in gray in Figure 3B. Here, the integral window was carefully designed to maximize both reliability and sensitivity in detecting spectral shifts. The end position of the integration window was set at the transmission maximum of the bare GMR chip's response, while the starting position was chosen at the transmission minimum. This configuration ensures that the integration captures consistent spectral features of the resonance while avoiding regions where intensity fluctuations

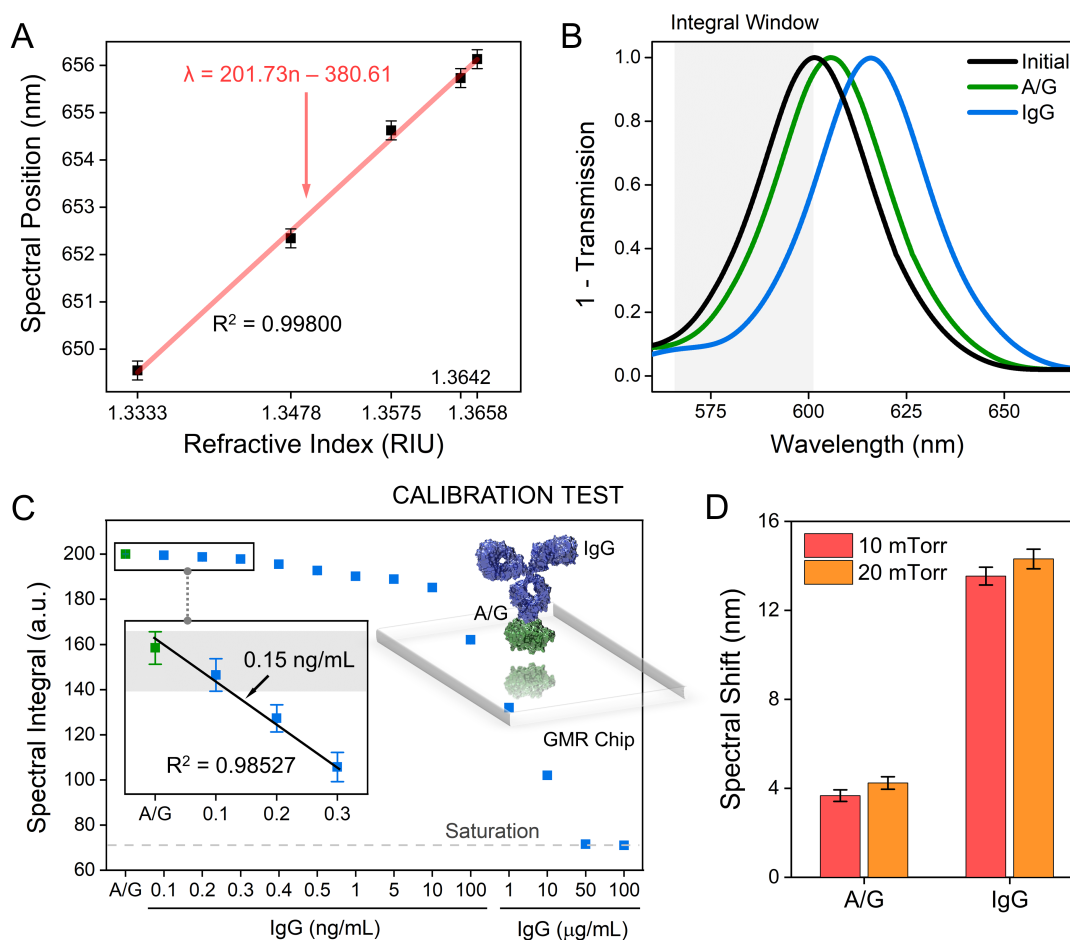


**Fig. 3.** (A) Spectral position of the transmission resonance supported by the GMR structure for different refractive indices of bulk solutions containing mixtures of DI-water and ethanol with varying ratios from 0 to 80%. The linear fit to the experimental data is shown in red. (B) Transmission resonance of the GMR structure: initial (black curve), after the attachment of 100  $\mu$ g/mL protein A/G (green curve), and after the attachment of 100  $\mu$ g/mL protein IgG (blue curve). The gray rectangle denotes the spectral range used for calculating the integral of the transmission spectrum. (C) Spectral integral values calculated for protein IgG concentrations ranging from 0.1 ng/mL to 100  $\mu$ g/mL (blue squares) and the values calculated for protein A/G (green square). A zoomed-in image corresponds to a smaller portion of the IgG concentration range, highlighting the system's LOD. The system LOD was determined as 0.15 ng/mL (highlighted with an arrow) using the LOD formula for the parameters determined from the linear regression model fitted to the experimental data. Gray area shows the overlapping spectral integral values, while surface saturation is indicated by the dashed gray line. (D) Spectral shift amounts for 100  $\mu$ g/mL protein A/G and 100  $\mu$ g/mL protein IgG for the GMR structures fabricated at 10 mTorr (red bars) and 20 mTorr (orange bars). In the figures, the squares and the bars represent the averages of the data obtained from five independent experiments, with error bars indicating double the standard deviation.

could compromise the reliability of the calculations. Importantly, the integration window primarily focuses on spectral shifts occurring on the right shoulder of the transmission resonance. Here, including other parts of the resonance, such as the left shoulder, could introduce variability due to fluctuations in the transmission curve, particularly where transmission intensity increases and decreases near the resonance peak. Such variability would compromise calculation accuracy. Additionally, the spectral minimum at the starting position of the integration window remains stable across a broad wavelength range, making it less sensitive to external noise or unrelated spectral features. This carefully selected configuration ensures that only consistent spectral changes directly related to the resonance are considered, enhancing the robustness, precision, and reliability of the sensing process.

The spectral integral method employed in our study en-

ables the monitoring of multiple wavelength points within a predefined spectral window, offering a significant advantage over methods that rely solely on a single peak or point. This approach captures cumulative changes across the spectral range, ensuring that valuable information is retained, even when some spectral shifts fall below the instrument's resolution. By integrating the response over a broader spectral window, the method effectively compensates for potential resolution limitations and leverages the majority of detectable shifts within the defined range. This ensures that even subtle resonance shifts, which are critical for biosensing applications, contribute meaningfully to the sensing process. As a result, the spectral integral method enhances both the sensitivity and reliability of our platform, while maintaining robustness against noise and variability. This makes it a highly effective strategy for accurate and reliable detection of biomolecular

interactions.

Figure 3C shows the spectral integral values obtained for various concentrations of protein IgG, ranging from 0.1 ng/mL to 100  $\mu\text{g/mL}$  (blue squares). As the analyte concentration increases, it induces a spectral separation of the transmission resonance within the specified window, resulting in a decrease in the integral value. As depicted in the figure, at a protein IgG concentration of 50  $\mu\text{g/mL}$ , the spectral integral values saturate (no variation is observed beyond this concentration) due to the surface saturation with the targeted analytes (indicated by the dashed gray line). To offer a more detailed examination of IgG concentrations between 0 and 0.3 ng/mL, where 0 concentration corresponds to the transmission resonance of the waveguide coated exclusively with protein A/G (green square), we have included a zoomed-in inset within Figure 3C. In this inset, the squares denote the average spectral integral values derived from five independent experiments, with the error bars indicating double the standard deviation. Notably, the integral value corresponding to 0.2 ng/mL of protein IgG can be reliably distinguished from 0 and 0.1 ng/mL concentrations, as highlighted in gray. To determine the exact limit of detection (LOD) for our system, we applied a linear regression model that yielded an  $R^2$  value of 0.98527. This allowed us to establish the Limit of Detection (LOD) for our biosensor system. The LOD was calculated using the formula  $\text{LOD} = 3.3\sigma/s$ , where  $\sigma$  represents the standard deviation of the signal, and  $s$  represents the slope of the calibration curve [31]. We determined the system LOD to be 0.15 ng/mL for protein IgG as highlighted with an arrow in the figure. This LOD represents a significant step in highly sensitive binding dynamic analysis towards commercial applications, e.g., SPR technologies offer a sensitivity range between 10 and 100  $\mu\text{g/mL}$  [32].

While GMR sensors generally exhibit lower refractive index sensitivity and higher LOD compared to SPR sensors, they are still widely adopted in the field due to several inherent advantages [36]. GMR sensors compensate for this limitation with other strengths that make them highly desirable for specific applications. For instance, GMR sensors benefit from narrow spectral bandwidths, often achieving full-width at half-maximum (FWHM) values that are orders of magnitude smaller than those of SPR sensors. This feature enhances the figure of merit (FOM) of GMR sensors, enabling precise detection of refractive index changes even with modest sensitivity. Another significant advantage of GMR sensors lies in their robust dielectric-based construction, which imparts superior thermal and chemical stability. Unlike SPR sensors, which rely on metallic nanostructures prone to degradation under high temperatures or corrosive environments, GMR sensors can maintain consistent performance under demanding conditions. This makes them particularly suitable for applications involving harsh environments or long-term monitoring. Furthermore, GMR sensors are highly adaptable to various configurations, supporting operation in both transmission and reflection modes, and they integrate with microfluidic platforms, enabling advanced applications such as in situ monitoring of chemical or biochemical reactions. Additionally, the fabrication of GMR sensors using techniques like atomic layer deposition (ALD) allows for precise control over sensor

architecture, enabling the production of highly uniform and reproducible nanostructures at a relatively low cost. This scalability and reproducibility further position GMR sensors as an attractive alternative to SPR, especially in applications where cost-effectiveness, integration into complex systems, and robustness are prioritized. While SPR remains the gold standard for achieving the lowest LODs, GMR's unique combination of stability, versatility, and precision makes it a valuable tool in optical sensing and biosensing applications, particularly for scenarios requiring high durability and flexible system design.

### C. Effect of the Operational Pressure of the Nanofabrication on GMR Sensitivity

In this section, we conducted a comparison of the sensing capabilities between our waveguide systems fabricated at 10 mTorr (red bars) and 20 mTorr (orange bars). Figure 3D presents the spectral shift amounts for two proteins: 100  $\mu\text{g/mL}$  protein A/G and 100  $\mu\text{g/mL}$  protein IgG. The bars correspond to the average of the data collected from five independent experiments, with error bars reflecting twice the standard deviation. The results illustrate that the system fabricated at 20 mTorr supports higher sensitivity when contrasted with the one produced at 10 mTorr. This disparity could be attributed to the fact that an oxygen pressure of 20 mTorr yields higher porosity, resulting in a greater surface area, for  $\text{TaO}_2$ , as opposed to the 10 mTorr condition. A greater sensing surface area significantly enhances the performance of label-free biosensing, primarily due to its capacity to capture more analytes from the targeted sample. This attribute is crucial for detecting low-abundance targets as it substantially increases the likelihood of these molecules being captured and detected. With more available space for biomolecules to bind, the sensor not only ensures a stronger signal for the same concentration of analyte, thereby increasing sensitivity but also improves the overall reliability and reproducibility of the detection process. This enhanced capacity for biomolecule binding allows for the sensor to be functionalized with a larger number of recognition elements, which can be tailored to specifically bind to target analytes. As a result, the selectivity of the sensor is improved, enabling it to more effectively distinguish target molecules from non-targets.

### D. Assessing Binding Dynamics with the GMR Platform

Our technology incorporates microfluidics, i.e., it allows monitoring biomolecular binding events. For targeted delivery of analytes, we manufactured a PDMS based flow cell via CNC-drilling [33]. The schematic and the photograph of the CNC-drilled mold are presented in Figure 4C, which was manufactured for the device parameters of,  $L = 15.7$  mm and  $W = 3.4$  mm, on a 1.6-mm-thick FR4 plate coated with a thin copper film. Figure 4D shows the photograph of the one-channel flow cell bonded to the GMR chip. Here, as the CNC drilling left marks on the mold, the PDMS surface became uneven, and plasma activation was not utilized. Instead, a thin layer of liquid PDMS was applied to the bottom of the PDMS surface, and then placed on the GMR chip. The PDMS layer was cured at 70  $^\circ\text{C}$  to ensure a secure bond. This technique

enables the realization of PDMS-based microfluidics without the need for the lithography-based techniques requiring sophisticated cleanroom infrastructure.

As a proof-of-principle demonstration, we examined the interactions between protein A/G and protein IgG. To achieve this, we introduced a solution containing protein IgG over the GMR surface, which is coated with protein A/G, leading to the formation of the IgG-A/G protein complex. The binding between these two proteins is influenced by the association ( $k_a$ ) and disassociation ( $k_d$ ) constants, and the kinetics of their molecular interaction over time were analyzed using a model based on reference [34]:

$$\frac{d[\text{IgG-A/G}]}{dt} = k_a[\text{IgG}][\text{A/G}] - k_d[\text{IgG-A/G}] \quad (2)$$

where the disassociation constant for the interaction between protein A/G and protein IgG is a value of  $k_d < 10^{-6}$  (1/s) [35]. The rate of change in the spectral integral is directly linked to the formation of the IgG-A/G protein complex. To gain insights into the relationship between the binding rates, we analyzed the integral of the time-dependent molecular interaction kinetic:

$$SI(t) = \frac{k_a[\text{IgG}]SI_{\max}}{k_a[\text{IgG}] + k_d} \times \frac{1}{1 + e^{(k_a[\text{IgG}] - k_d)t}} \quad (3)$$

where  $SI_{\max}$  is the maximum spectral integral value associated with the GMR surface saturated with protein IgG, and  $SI(t)$  is the change in the spectral integral at time  $t$ . Arranging the terms yields,

$$SI(t) = \frac{SI_0}{1 + e^{Ct}} \quad (4)$$

where

$$C = k_a[\text{IgG}] - k_d \quad (5)$$

and

$$SI_0 = \frac{k_a[\text{IgG}]\Delta I_{\max}}{k_a[\text{IgG}] + k_d} \quad (6)$$

where  $[\text{IgG}]$  represents the concentration of protein IgG. Given that in this context,  $k_a[\text{IgG}]$  significantly exceeds  $k_d$ , the exponential constant is directly related to a factor represented as  $C$ , which can be expressed as  $C = k_a[\text{IgG}]$ .

In Figure 4E, we show the dynamic changes in the spectral integral observed during the interaction between protein IgG and A/G over a 1-hour time period. Initially, the surface was functionalized with a high concentration of protein A/G (100  $\mu\text{g/mL}$ ) to ensure complete saturation of the biosensing surface with the capturing agent. This saturation guarantees effective analyte capture by the surface-bound ligand even at extremely low analyte concentrations, which is critical for robust real-time binding kinetics applications. Following this initial phase, protein IgG was introduced onto the sensor surface for interaction with a flow rate of 0.1 mL/min. The increase in the biomass on the sensing surface resulted in an exponential decrease in the spectral integral. Once the sensing surface became saturated at  $t = \sim 30$  min. (denoted with a black dashed line in Figure 4E), further changes in intensity ceased. Using our exponential model (red curve) fitted to the

experimental data (gray curve), we determined the association constant ( $k_a$ ) for protein IgG with a molecular weight of 160 kDa to be  $k_a = 3.65 \times 10^5$  (1/Ms). Remarkably, this calculated value closely corresponds to the literature-reported value of  $k_a = 3.11 \times 10^5$  (1/Ms) [35]. This suggests a strong agreement between our experimental findings and existing data, affirming the reliability of our biosensing system in characterizing the protein-protein interaction dynamics. As an additional note, temperature fluctuations play a significant role in optical biosensing, influencing refractive index variations and, subsequently, the observed binding kinetics. Such thermal effects are commonly encountered in systems like SPR and are similarly observed in our platform. To address this, we conducted all binding kinetics experiments under controlled laboratory conditions. For extended applications, incorporating active temperature regulation, such as thermoelectric cooling or a temperature-controlled stage, could further enhance stability.

### E. Software Module

To facilitate the integrated operation of the hardware system from a single panel and to generate binding dynamics information by processing spectral data, we have developed a Python-based GUI, as depicted in Figure 5. Upon initiating the program, the GUI interfaces with the spectrometer system through its dynamic-link library (DLL) files, presenting the real-time transmission spectrum in the top-left panel. Given our utilization of three spectrometers, the GUI displays three distinct spectra, each denoted with a unique color (blue, green and red), all within the visible spectral range. The figure shows the raw transmission data before applying any processing options supported by the system GUI. For robust data processing, the GUI enables the operator to perform various actions, e.g., the *Normalize* command is for normalization of the GMR response by the source spectrum, where the *Source* command captures the spectrum of the halogen source. Additionally, the *Inverse* command is employed to derive the 1-Transmission spectrum. The *Find Window* command assists in positioning the spectral integration window, highlighted with a yellow rectangular box on the transmission spectrum within the same panel. The *Spectrometer Settings* panel, located in the bottom-left section, grants the operator the ability to specify interaction times, which dictate the duration for spectrometers to collect photons at each goniometer measurement point, e.g., *Integration Time (msec)* for each spectrometer. Raw data may be further refined through the application of the *Boxcar Width* command. The manufacturer-defined boxcar averaging function for spectral data smoothing depends on the boxcar width parameter. This parameter governs the extent of pixel inclusion on both sides of the central pixel, ultimately determining the number of pixels encompassed in the average, e.g., *Pixels Averaged* =  $2 \times \text{Boxcar Width} + 1$ . As shown the figure, GUI simultaneously shows the smoothen spectra (white curve) with the raw data. In the *Pump Settings* panel, situated in the middle section, the operator has the capability to select, initiate or stop the pump's operation via the *Start Pump* and *Stop Pump* commands, specifying the desired *Flow Rate (mL/min)* and *Duration (sec)*.

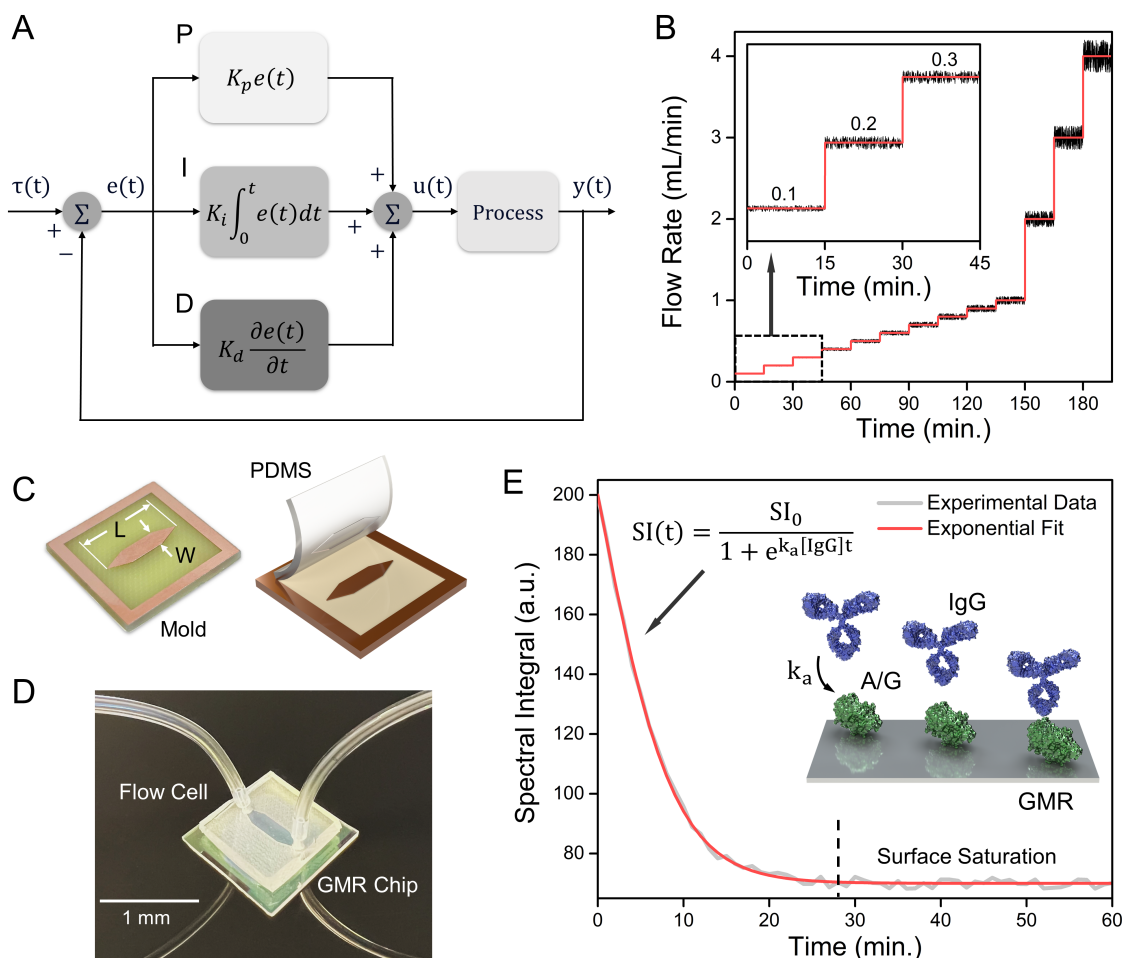


**Fig. 4.** (A) The schematic illustration of the first order system modelling the PID controller for controlling the flow rate. (B) Flow rate values (black) measured with the flow sensor for the set values (red). Figure inset zooms into the flow rates, 0.1, 0.2 and 0.3 mL/min. (C) Photograph and schematic of the mold used to manufacture the PMDS-based one-channel flow cell. (D) Photograph of the flow cell bonded to the GMR chip. (E) The exponential change in the spectral integral value calculated for a GMR chip coated with protein A/G, when 100  $\mu$ g/mL protein IgG is flowed over the surface for a duration of 1 hour.

Upon clicking the *Start Pump* icon, the chosen piezoelectric pump, the associated valve, and the flow sensor are activated simultaneously. Within the *Test Parameters* panel, pertaining to analyte parameters, the operator can provide either the molarity  $M$  (mol/L), or concentration ( $\mu$ g/mL) along with the molecular weight  $MW$  (kDa). The operator also defines the *Time Interval* (sec) for each data point. Executing the *Run Test* operation, the GUI calculates the integral within the spectral integration window (determined by the *Find Window* function) for each time interval for the parameters provided by the operator in the *Spectrometer Settings* and *Pumps Settings* panels. Throughout the test, the GUI provides the real-time updates of the calculated spectral integral values in the top-right panel. After the test duration concludes, the GUI automatically computes and displays the “ $k_a$ ” value on the same graph. Furthermore, the operator has the option to save the calculated spectral integral vs. time data (*Save Integral*) or the raw spectrum data for each time interval (*Save Spec*), as well as the ability to recall spectral interval or raw spectral data using the *Export Data* icon. System software facilitates the execution of

protocols (*Run Protocol* panel) with multiple steps, including surface cleaning, surface functionalization, and biomolecular interaction. Here, the operator can choose the number of steps and the solutions, along with their associated pumps, to be used in the sequential steps. For each step, the operators can define the flow rate and the duration for running the pumps. The operator can also select the steps where spectrometers are utilized to gather spectral data and conduct data processing to determine the binding parameters afterwards. Figure 5 shows an example of a comprehensive step-by-step analysis of the interaction between protein A/G and protein IgG within our platform, which encompasses five distinct phases. Initially, the surface is prepared through cleaning with phosphate buffered saline (PBS) at a flow rate of 3  $\mu$ L/min for a duration of 5 min. This is followed by the surface functionalization using protein A/G, applied at a minimal flow rate of 0.1  $\mu$ L/min for 60 min. Post-functionalization, any unbound proteins are washed off the surface using PBS at a flow rate of 0.5  $\mu$ L/min for 5 min. To facilitate robust biomolecular binding, protein IgG is subsequently introduced over the GMR surface coated with

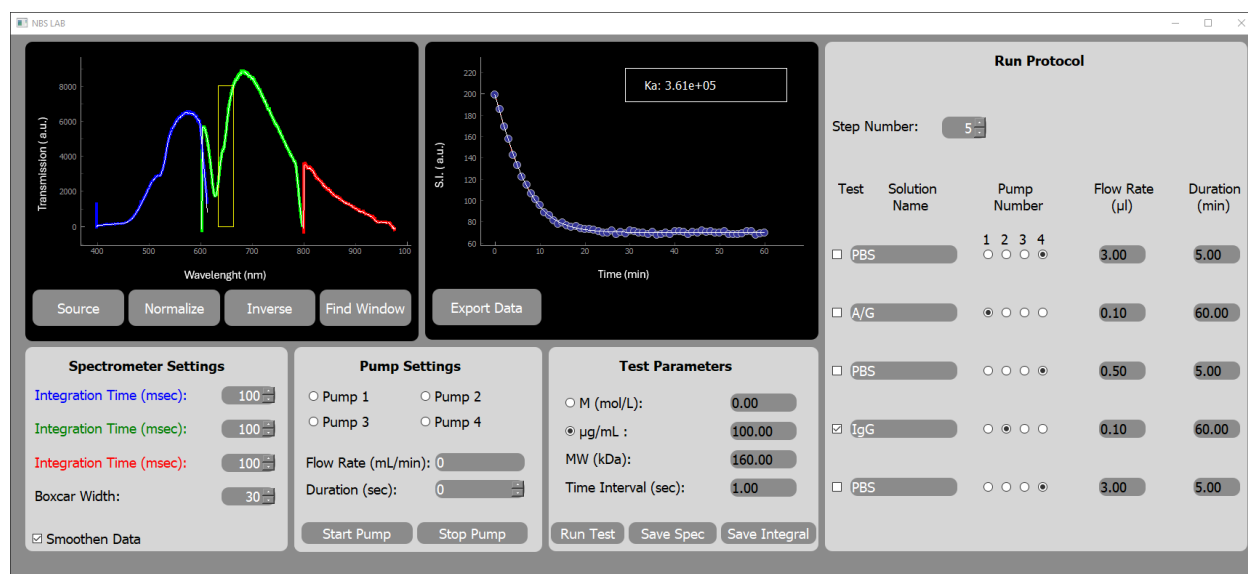


Fig. 5. Python-based system software operating hardware components and processing raw spectral data to provide binding kinetics information to the operator. The GUI also supports the execution of protocols in a fully automated manner for surface functionalization, biomolecular binding, and system cleaning.

protein A/G, maintained at a slow flow rate of 0.1  $\mu\text{L}/\text{min}$  for 60 min. The protocol concludes with a final PBS wash at a flow rate of 3  $\mu\text{L}/\text{min}$  for 5 min, aimed at cleansing the components of the Microfluidics Module, including tubing and PDMS layers. Notably, spectral measurements and the calculation of binding parameters were conducted during the fourth step (*Test* icon is selected), providing critical data on the biomolecular interactions. Here, the PBS container was connected to the last pump (Pump #4) to ensure that PBS cleanses the interior of the manifold from the beginning, thereby eliminating any potential cross-contamination.

#### IV. CONCLUSION

In conclusion, we introduced an optofluidic GMR platform that provides a fully automated and comprehensive solution for label-free and real-time analysis of biomolecular interactions. The platform integrates advanced features, including an inverted microscopy system with linearly polarized illumination, a high-resolution multi-spectrometer setup, and a precision-controlled multi-pump system, ensuring high accuracy and efficiency in biosensing assays. By automating critical flow processes such as chip preparation, ligand and analyte incubation, and self-cleaning, the platform minimizes manual labor and reduces the risk of human error, resulting in consistent and reliable experimental outcomes. Additionally, the user-friendly software developed for this platform enhances its operational functionality, facilitating seamless control over optofluidic components and enabling efficient data acquisition, analysis, and detailed examination of binding kinetics. This integrated system not only provides valuable insights into biomolecular dynamics but also paves the way for significant advancements in diagnostic research and bioanalytical applications. Furthermore, the platform's optical transmission-based capabilities allow for compatibility with diverse photonic chip technologies, including photonic crystals, plasmonic structures, and

waveguides. This versatility expands the potential applications of the technology across a variety of fields, offering a powerful tool for future innovations in biosensing and beyond.

#### ACKNOWLEDGMENT

This work was supported by the Development of International Cooperation Network on Science Technology and Innovation, Program Management Unit for Human Resources & Institutional Development, Research and Innovation (PMU-B) of Thailand (which is under the Program 16: Partnership Initiative Fund: S&T) Grant No. B16F640194, National Higher Education Science Research and Innovation Policy Council.

#### REFERENCES

- [1] Y. Zhou, B. Wang, Z. Guo, and X. Wu, "Guided Mode Resonance Sensors with Optimized Figure of Merit," *Nanomaterials*, vol. 9, no. 6, p. 837, 2019. <https://doi.org/10.3390/nano9060837>.
- [2] R. Magnusson, D. Wawro, S. Zimmerman, and Y. Ding, "Resonant Photonic Biosensors with Polarization-Based Multiparametric Discrimination in Each Channel," *Sensors*, vol. 11, no. 2, pp. 1476–1488, 2011. <https://doi.org/10.3390/s110201476>.
- [3] R. Magnusson and S. S. Wang, "New Principle for Optical Filters," *Appl. Phys. Lett.*, vol. 61, no. 9, pp. 1022–1024, 1992. <https://doi.org/10.1063/1.107703>.
- [4] S. Tibuleac, D. Wawro, and R. Magnusson, "Resonant Diffractive Structures Integrating Waveguide-Gratings on Optical Fiber Endfaces," in *1999 IEEE LEOS Annual Meeting Conference Proceedings. LEOS'99. 12th Annual Meeting*, IEEE Lasers and Electro-Optics Society, vol. 2, pp. 874–875, 1999. <https://doi.org/10.1109/LEOS.1999.812013>.
- [5] D. D. Wawro, S. Tibuleac, R. Magnusson, and H. Liu, "Optical Fiber Endface Biosensor Based on Resonances in Dielectric Waveguide Gratings," in *3911*, T. Vo-Dinh, W. S. Grundfest, and D. A. Benaron, Eds., *Proc. SPIE*, pp. 86–94, 2000. <https://doi.org/10.1117/12.384889>.
- [6] M. Maleki and M. Mehran, "Guided-Mode Resonance Sensors: Different Schemes for Different Applications," *J. Opt. Soc. Am. B*, vol. 39, no. 6, p. 1634, 2022. <https://doi.org/10.1364/JOSAB.449373>.
- [7] H. Kikuta, N. Maegawa, A. Mizutani, K. Iwata, and H. Toyota, "Refractive Index Sensor with a Guided-Mode Resonant Grating Filter," in *4416*, K. Iwata, Ed., *Proc. SPIE*, p. 219, 2001. <https://doi.org/10.1117/12.427053>.

- [8] B. Cunningham, P. Li, B. Lin, and J. Pepper, "Colorimetric Resonant Reflection as a Direct Biochemical Assay Technique," *Sensors Actuators B Chem.*, vol. 81, no. 2–3, pp. 316–328, 2002. [https://doi.org/10.1016/S0925-4005\(01\)00976-5](https://doi.org/10.1016/S0925-4005(01)00976-5).
- [9] B. Cunningham, J. Qiu, B. Lin, P. Li, and J. Pepper, "A Plastic Colorimetric Resonant Optical Biosensor for Multiparallel Detection of Label-Free Biochemical Interactions," in *Proceedings of IEEE Sensors*, IEEE, vol. 1, pp. 212–216. <https://doi.org/10.1109/ICSENS.2002.1037084>.
- [10] Y. Fang, A. M. Ferrie, and G. Li, "Probing Cytoskeleton Modulation by Optical Biosensors," *FEBS Lett.*, vol. 579, no. 19, pp. 4175–4180, 2005. <https://doi.org/10.1016/j.febslet.2005.06.050>.
- [11] Y. Fang, A. Frutos, and R. Verklereen, "Label-Free Cell-Based Assays for GPCR Screening," *Comb. Chem. High Throughput Screen.*, vol. 11, no. 5, pp. 357–369, 2008. <https://doi.org/10.2174/138620708784534789>.
- [12] W. Liu, J. Yan, and Y. Shi, "High Sensitivity Visible Light Refractive Index Sensor Based on High Order Mode Si<sub>3</sub>N<sub>4</sub> Photonic Crystal Nanobeam Cavity," *Opt. Express*, vol. 25, no. 25, p. 31739, 2017. <https://doi.org/10.1364/OE.25.031739>.
- [13] W.-K. Kuo, J.-X. Lin, J. Tongpakpanang, and D.-S. Liu, "Guided-Mode Resonance Pressure Sensor Based on a Stretchable Low-Density Polyethylene Film," *Appl. Opt.*, vol. 61, no. 21, p. 6223, 2022. <https://doi.org/10.1364/AO.460237>.
- [14] K. Wu, D. Tonini, S. Liang, R. Saha, V. K. Chugh, and J.-P. Wang, "Giant Magneto-resistance Sensors in Biomedical Applications," *ACS Appl. Mater. Interfaces*, vol. 14, no. 8, pp. 9945–9969, 2022. <https://doi.org/10.1021/acsmi.1c20141>.
- [15] A. Kenaan, K. Li, I. Barth, S. Johnson, J. Song, and T. F. Krauss, "Guided Mode Resonance Sensor for the Parallel Detection of Multiple Protein Biomarkers in Human Urine with High Sensitivity," *Biosens. Bioelectron.*, vol. 153, p. 112047, 2020. <https://doi.org/10.1016/j.bios.2020.112047>.
- [16] B. Xu, Y. Fang, S. Li, Y. Huang, X. Cheng, Z. Li, and P. Tan, "A Novel Method for Fabricating Guided-Mode Resonance Filters by Dip-Coating Colloidal Nanospheres," *Optik (Stuttg.)*, vol. 272, p. 170299, 2023. <https://doi.org/10.1016/j.ijleo.2022.170299>.
- [17] G. Y. Sung, W.-J. Kim, H. Ko, B. K. Kim, K.-H. Kim, C. Huh, and J. Hong, "Portable Guided-Mode Resonance Biosensor Platform for Point-of-Care Testing," in H. Mohseni, M. H. Agahi, and M. Razeghi, Eds., 2012, p. 84600F. <https://doi.org/10.1117/12.929457>.
- [18] M. G. Abdallah, J. A. Buchanan-Vega, K. J. Lee, B. R. Wenner, J. W. Allen, M. S. Allen, S. Gimlin, D. W. Weidanz, and R. Magnusson, "Quantification of Neuropeptide Y with Picomolar Sensitivity Enabled by Guided-Mode Resonance Biosensors," *Sensors*, vol. 20, no. 1, p. 126, 2019. <https://doi.org/10.3390/s20010126>.
- [19] G. J. Triggs, Y. Wang, C. P. Reardon, M. Fischer, G. J. O. Evans, and T. F. Krauss, "Chirped Guided-Mode Resonance Biosensor," *Optica*, vol. 4, no. 2, p. 229, 2017. <https://doi.org/10.1364/OPTICA.4.000229>.
- [20] G. Finco, M. Z. Bideskan, L. Vertchenko, L. Y. Beliaev, R. Malureanu, L. R. Lindvold, O. Takayama, P. E. Andersen, and A. V. Lavrinenko, "Guided-Mode Resonance on Pedestal and Half-Buried High-Contrast Gratings for Biosensing Applications," *Nanophotonics*, vol. 10, no. 17, pp. 4289–4296, 2021. <https://doi.org/10.1515/nanoph-2021-0347>.
- [21] J. Yu, T. Zhang, Q. Wulan, L. Xing, Z. Li, and Z. Liu, "Guided-Mode Resonance with Reduced Bandwidth in Mid-Infrared Absorption and Thermal Emission," *Appl. Opt.*, vol. 61, no. 20, p. 5869, 2022. <https://doi.org/10.1364/AO.461292>.
- [22] I. Yamada, "Fabrication of Cu Grating Guided-Mode Resonance Filter by Electroplating," *Appl. Phys. Express*, vol. 16, no. 7, p. 072002, 2023. <https://doi.org/10.35848/1882-0786/ace14f>.
- [23] S. Sarkar, V. Gupta, M. Kumar, J. Schubert, P. T. Probst, J. Joseph, and T. A. F. König, "Hybridized Guided-Mode Resonances via Colloidal Plasmonic Self-Assembled Grating," *ACS Appl. Mater. Interfaces*, vol. 11, no. 14, pp. 13752–13760, 2019. <https://doi.org/10.1021/acsmi.8b20535>.
- [24] R. L. Rich and D. G. Myszka, "Survey of the Year 2000 Commercial Optical Biosensor Literature," *J. Mol. Recognit.*, vol. 14, no. 5, pp. 273–294, 2001. <https://doi.org/10.1002/jmr.547>.
- [25] M. J. Cannon, G. A. Papalia, I. Navratilova, R. J. Fisher, L. R. Roberts, K. M. Worthy, A. G. Stephen, G. R. Marchesini, E. J. Collins, D. Casper, H. Qiu, D. Satpaev, S. F. Liparoto, D. A. Rice, I. I. Gorshkova, R. J. Darling, D. B. Bennett, M. Sekar, E. Hommema, A. M. Liang, E. S. Day, J. Inman, S. M. Karlicek, S. J. Ullrich, T. Chu, E. Sullivan, J. Simpson, A. Rafique, B. Luginbühl, S. N. Westin, M. Bynum, P. Cachia, Y.-J. Li, D. Kao, A. Neurauter, M. Wong, M. Swanson, and D. G. Myszka, "Comparative Analyses of a Small Molecule/Enzyme Interaction by Multiple Users of Biacore Technology," *Anal. Biochem.*, vol. 330, no. 1, pp. 98–113, 2004. <https://doi.org/10.1016/j.ab.2004.02.027>.
- [26] N. Srisuai, C. Chananonawathorn, B. Seeleang, K. Tantiwanichapan, T. Lertvanithpol, A. Sathukarn, T. Pogfay, K. Jaruwongrungee, M. Horprathum, and S. Boonruang, "A Nanocolumnar Tantalum Oxide-Guided Mode Resonance Sensor for Volatile Organic Compounds," *ACS Appl. Nano Mater.*, vol. 4, no. 9, pp. 9665–9672, 2021. <https://doi.org/10.1021/acsnm.1c02054>.
- [27] K. Tantiwanichapan, R. Jolivot, A. Jomphoak, N. Srisuai, C. Chananonawathorn, T. Lertvanithpol, M. Horprathum, and S. Boonruang, "Author Correction: Demonstration of Cross Reaction in Hybrid Graphene Oxide/Tantalum Dioxide Guided Mode Resonance Sensor for Selective Volatile Organic Compound," *Sci. Rep.*, vol. 13, no. 1, p. 13677, 2023. <https://doi.org/10.1038/s41598-023-40864-5>.
- [28] M. Soler and L. M. Lechuga, "Biochemistry Strategies for Label-Free Optical Sensor Biofunctionalization: Advances towards Real Applicability," *Anal. Bioanal. Chem.*, vol. 414, no. 18, pp. 5071–5085, 2022. <https://doi.org/10.1007/s00216-021-03751-4>.
- [29] A. E. Cetin, D. Etezadi, B. C. Galarreta, M. P. Busson, Y. Eksioğlu, and H. Altug, "Plasmonic Nanohole Arrays on a Robust Hybrid Substrate for Highly Sensitive Label-Free Biosensing," *ACS Photonics*, vol. 2, no. 8, pp. 1167–1174, 2015. <https://doi.org/10.1021/acsp Photonics.5b00242>.
- [30] A. E. Cetin, S. N. Topkaya, O. Yalcin-Ozuyul, and A. Khademhosseini, "Refractive Index Sensing for Measuring Single Cell Growth," *ACS Nano*, 2021. <https://doi.org/10.1021/acsnano.1c04031>.
- [31] D. A. Armbruster and T. Pry, "Limit of Blank, Limit of Detection and Limit of Quantitation," *Clin. Biochem. Rev.*, vol. 29, Suppl 1, pp. S49–S52, 2008.
- [32] H. Nguyen, J. Park, S. Kang, and M. Kim, "Surface Plasmon Resonance: A Versatile Technique for Biosensor Applications," *Sensors*, vol. 15, no. 5, pp. 10481–10510, 2015. <https://doi.org/10.3390/s150510481>.
- [33] S. Yaman, M. B. Avci, F. Kurul, S. N. Topkaya, and A. E. Cetin, "Hand-held Optofluidic Platform towards Binding Dynamics Applications in Field-Settings," *Sensors Actuators A Phys.*, vol. 363, p. 114685, 2023. <https://doi.org/10.1016/j.sna.2023.114685>.
- [34] K. Saha, F. Bender, and E. Gizeli, "Comparative Study of IgG Binding to Proteins G and A: Nonequilibrium Kinetic and Binding Constant Determination with the Acoustic Waveguide Device," *Anal. Chem.*, vol. 75, no. 4, pp. 835–842, 2003. <https://doi.org/10.1021/ac0204911>.
- [35] V. Bronner, M. Tabul, and T. Bravman, "Rapid Screening and Selection of Optimal Antibody Capturing Agents Using the ProteOn XPR36 Protein Interaction Array System," *Bio-Rad Tech. Note*, vol. 5820, 2006.
- [36] A. Szeghalmi, E. B. Kley, Mato Knez, "Theoretical and Experimental Analysis of the Sensitivity of Guided Mode Resonance Sensors," *J. Phys. Chem. C*, vol. 14, no. 49, pp. 21150–21157, 2010. <https://doi.org/10.1021/jp107540y>.
- [37] C. T. Yeh, D. Barshilia, C. J. Hsieh, H. Y. Li, W. H. Hsieh, and G. E. Chang, "Rapid and highly sensitive detection of C-reaction protein using robust self-compensated guided-mode resonance biosensing system for point-of-care applications," *Biosensors*, vol. 11, no. 12, p. 523, 2021. <https://doi.org/10.3390/bios11120523>.
- [38] Z. Vafapour and A. Zakery, "New regime of plasmonically induced transparency," *Plasmonics*, vol. 10, pp. 1809–1815, 2015. <https://doi.org/10.1007/s11468-015-9992-4>.
- [39] Z. Vafapour, H. Ghahraloud, A. Keshavarz, M. S. Islam, A. Rashidi, M. Dutta, and M. A. Stroschio, "The potential of refractive index nanobiosensing using a multi-band optically tuned perfect light metamaterial absorber," *IEEE Sensors Journal*, vol. 21, no. 12, pp. 13786–13793, 2021. <https://doi.org/10.1109/JSEN.2021.3070731>.
- [40] Z. Vafapour and H. Alaei, "Subwavelength micro-antenna for achieving slow light at microwave wavelengths via electromagnetically induced transparency in 2D metamaterials," *Plasmonics*, vol. 12, pp. 1343–1352, 2017. <https://doi.org/10.1007/s11468-016-0392-1>.
- [41] S. Xia, X. Zhai, L. Wang, and S. Wen, "Plasmonically induced transparency in in-plane isotropic and anisotropic 2D materials," *Optics Express*, vol. 28, no. 6, pp. 7980–8002, 2020. <https://doi.org/10.1364/OE.389573>.
- [42] J. Wu, B. Dai, Z. Li, T. Pan, D. Zhang, and F. Lin, "Emerging optofluidic technologies for biodiagnostic applications," *View*, vol. 2, no. 4, p. 20200035, 2021. <https://doi.org/10.1002/VIW.20200035>.
- [43] S. Xia, X. Zhai, L. Wang, and S. Wen, "Plasmonically induced transparency in in-plane isotropic and anisotropic 2D materials," *Optics Express*, vol. 28, no. 6, pp. 7980–8002, 2020. <https://doi.org/10.1364/OE.389573>.
- [44] D. Ozcelik, H. Cai, K. D. Leake, A. R. Hawkins, and H. Schmidt, "Optofluidic bioanalysis: fundamentals and applications," *Nanophotonics*, vol. 6, no. 4, pp. 647–661, 2017. <https://doi.org/10.1515/nanoph-2016-0156>.

- [45] S. Xia, X. Zhai, L. Wang, Y. Xiang, and S. Wen, "Plasmonically induced transparency in phase-coupled graphene nanoribbons," *Physical Review B*, vol. 106, no. 7, p. 075401, 2022. <https://doi.org/10.1103/PhysRevB.106.075401>.
- [46] Z. Vafapour, H. Ghahraloud, A. Keshavarz, M. S. Islam, A. Rashidi, M. Dutta, and M. A. Stroschio, "The potential of refractive index nanobiosensing using a multi-band optically tuned perfect light metamaterial absorber," *IEEE Sensors Journal*, vol. 21, no. 12, pp. 13786–13793, 2021. <https://doi.org/10.1109/jsen.2021.3070731>.
- [47] G. Testa, G. Persichetti, and R. Bernini, "Optofluidic biosensing: devices, strategies, and applications," *TrAC Trends in Analytical Chemistry*, vol. 2024, p. 117865, 2024. <https://doi.org/10.1016/j.trac.2024.117865>.



**Chanunthorn Chananonawathorn** received the M.Sc. degree in Physics from Thammasat University, Bangkok, Thailand in 2015. She is now a research assistant at Opto-Electrochemical Sensing Research Team (OEC), National Electronics and computer technology center (NECTEC), Thailand. Her research interest includes metal oxide nanostructure, fabrications and characterization thin films technology, Surface enhance Raman spectroscopy and electrochromic materials.



**Meryem Beyza Avci** received the B.S. degree in Biomedical Engineering in 2021 and a double major B.S. degree in Mechatronics Engineering in 2022, both from the Izmir University of Economics, Turkey. She is currently pursuing the M.S. degree in Electrical and Electronics engineering at the same university. She is a researcher at the Izmir Biomedicine and Genome Center (IBG) in the Nanophotonics and Biodection Systems Laboratory, under the supervision of Dr. Arif E. Cetin. Her research inter-

ests include biosensing, optics, microfluidics, image processing, and nanophotonic devices.



**Tossaporn Lertvanithphol** received Ph.D. from King Mongkut's University of Technology Thonburi, Bangkok, Thailand in 2018. He is now a researcher at Opto-Electrochemical Sensing Research Team (OEC), National Electronics and computer technology center (NECTEC), Thailand. His research interest includes thin film fabrication and characterization, spectroscopic ellipsometry, Surface enhance Raman spectroscopy and plasmonic sensors.



**Furkan Kocer** received his bachelor's degree in Biomedical Engineering from Izmir Democracy University in 2023. He is currently pursuing his master's degree in Biomedical Engineering at Bakircay University. He is visiting researcher at the Izmir Biomedicine and Genome Center (IBG) in the Nanophotonics and Biodection Systems Laboratory, under the supervision of Dr. Arif E. Cetin. He focuses on recent advances in image processing, biological sensing and software development. His professional interests include de-

signing innovative solutions for biomedical applications and advancing technologies at the intersection of biology and engineering.



**Mati Horprathum** received Ph.D. degree in Physics from King Mongkut's University of Technology Thonburi (KMUTT), Thailand in 2009. He did his 1-year postdoctoral study at Laboratory of Atomic Scale Materials Processing, Institute of Scientific and Industrial Research (ISIR), Osaka University, Japan. He is now a senior researcher and the team leader of opto-electrochemical sensing research team (OEC), spectroscopic and sensing devices research unit, NECTEC, Thailand. His research interests

are nanostructure plasmonic sensor, optoelectronic devices, fabrications, and characterizations of nanostructures. In addition, he was awarded the 2016 ICO/ICTP Gallieno Denardo Award from the International Commission for Optics (ICO) and the Abdus Salam International Centre for Theoretical Physics (ICTP).



**Nimet Yildirim-Tirgil** received her B.Sc. degree in Biochemistry from Ege University, Turkey, in 2007. She earned her M.Sc. degree in Biochemistry from the Institute of Science at Ege University in 2009, with a thesis on the development of microbial biosensors. Dr. Yildirim Tirgil completed her Ph.D. in Bioengineering at Northeastern University, USA, in 2016, focusing on next-generation biosensor systems for environmental water quality monitoring. Since 2018, she has been serving as an Assistant

Professor in the Biomedical Engineering Department at Ankara Yildirim Beyazit University. Her research interests include the development of nanocomposite-based biosensors, electrochemical detection systems, and advanced diagnostic platforms for environmental and biomedical applications. Dr. Yildirim-Tirgil has authored numerous peer-reviewed publications, holds patents in biosensor technologies, and has been actively involved in national and international research projects. She is also the recipient of multiple research grants for her innovative work in biosensor development.



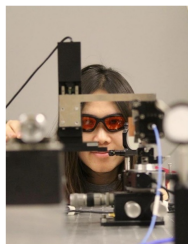
**Uraiwan Waiwijit** is a Senior Research Assistant in the Spectroscopic and Sensing Devices Research Group (SSDRG) at the National Electronics and Computer Technology Center (NECTEC), Thailand. She earned her B.Sc. and M.Sc. degrees in Medical Technology and Biochemistry from Chulalongkorn University in 2008 and 2010, respectively, and completed her Ph.D. in Nanotechnology from Asian Institute of Technology in 2021. Dr. Uraiwan's research focuses on the development of biosensors and

optical sensors, with an emphasis on immunoassays and the detection of biological molecules using advanced techniques such as surface-enhanced Raman scattering (SERS), guided-mode resonance (GMR), metal-enhanced fluorescence (MEF), and localized surface plasmon resonance (LSPR). She also has expertise in synthesizing optical nanomaterials and carbon-based materials for applications in electrochemical sensors.



**Sakoolkan Boonruang** graduated from the department of electrical engineering, King Mongkut Institute of Technology Ladkrabang, Thailand in 1999. In 2002, she joined the college of optics and photonics, CREOL, University of Central Florida, USA, as a graduate student. She received her Ph.D. degree in optics in 2007 with thesis titled “Two-dimensional Guided Mode Resonant Structures for Spectral Filtering Applications” under the supervision of Prof. M. G. Moharam. In the same year, she returned to

Thailand and joined the National Electronics and Computer Technology research center (NECTEC), where she is currently a researcher. Her current work focuses on fabrication of one/two dimensional periodical structures, optical sensors, VOCs sensor and biomedical optics applications.



**Khwanchai Tantiwanichapan** is a researcher in the Spectroscopic and Sensing Devices Research Group at the National Electronics and Computer Technology Center (NECTEC) in Thailand. He earned his M.S. and Ph.D. in Electrical Engineering from Boston University in 2016. Dr. Tantiwanichapan's current research centers on optical and Terahertz devices and sensors, with a focus on metamaterials, guided-mode resonance, and plasmonic materials.



**Arif E. Cetin** is a Group Leader in Izmir Biomedicine and Genome Center (IBG), Izmir, Turkey. Dr. Cetin received his BS degree in Electrical and Electronics Engineering and MS degree in Electrical and Computer Engineering both from Koc University, Istanbul, Turkey. He received his PhD degree in Electrical Engineering from Boston University, Boston, MA, USA. He worked as a postdoctoral associate at EPFL (Lausanne, Switzerland) and MIT (Cambridge, MA, USA), and as a research scientist at Om-

niome Inc. (San Diego, CA, USA). Dr. Cetin pursues research on optical nano-biosensors integrated with microfluidic platforms for ultra-sensitive label-free biodetection. He develops hand-held sensors for high-throughput and multiplexed biodetection in resource-poor settings. He also pursues research on growth rate cytometry for therapeutic profiling cancer cells and label-free techniques for high-throughput DNA sequencing.